

Article

Methylene Blue-Modified Biochar from Sugarcane for the Simultaneous Electrochemical Detection of Four DNA Bases

Qusai Hassan ^{1,2} , Zhixin Meng ¹ , Meissam Noroozifar ¹  and Kagan Kerman ^{1,2,*} 

¹ Department of Physical and Environmental Sciences, University of Toronto Scarborough, 1265 Military Trail, Toronto, ON M1C 1A4, Canada

² Department of Chemistry, University of Toronto, 80 St. George Street, Toronto, ON M5S 3H6, Canada

* Correspondence: kagan.kerman@utoronto.ca; Tel.: +1-(416)-287-7249

Abstract: The abnormal levels of four DNA bases, namely guanine (G), adenine (A), thymine (T), and cytosine (C) are implicated in several cancers, metabolic diseases, and HIV/AIDS. Therefore, the accurate detection and concentration measurement of these four DNA bases is of significant interest. Furthermore, there has recently been a push towards developing chemical sensors which are more sustainable and cost-effective. Herein, we developed a graphite paste electrode which incorporated the biochar of sugarcane and methylene blue (GPE-SC-MB) in order to simultaneously detect these four DNA bases. The linear ranges obtained for the four DNA bases are 0.67–38.67 μM for G, 0.67–126.67 μM for A, and 6.67–1600 μM for T and C. The limit-of-detection (LOD) values obtained were 0.037 μM for G, 0.042 μM for A, 4.25 μM for T, and 5.33 μM for C. The electroactive surface area of the electrode as well as the diffusion coefficients for each analyte were determined. Lastly, the GPE-SC-MB was tested in real samples using human saliva with recovery values between 99.0 and 103.0%. Thus, biochar from sugarcane proved to be an effective electrode modifier material for the development of sensitive electrochemical sensors.

Keywords: electrochemical sensor; methylene blue; DNA; modified electrode; biochar



Citation: Hassan, Q.; Meng, Z.; Noroozifar, M.; Kerman, K. Methylene Blue-Modified Biochar from Sugarcane for the Simultaneous Electrochemical Detection of Four DNA Bases. *Chemosensors* **2023**, *11*, 169. <https://doi.org/10.3390/chemosensors11030169>

Academic Editors: Alexander G. Bannov, Tamara Basova, Alexey Glushenkov and Mahmut Durmuş

Received: 20 January 2023

Revised: 21 February 2023

Accepted: 24 February 2023

Published: 1 March 2023



Copyright: © 2023 by the authors. Licensee MDPI, Basel, Switzerland. This article is an open access article distributed under the terms and conditions of the Creative Commons Attribution (CC BY) license (<https://creativecommons.org/licenses/by/4.0/>).

1. Introduction

Deoxyribonucleic acid (DNA) is the genetic code which underlies every living organism and is the first and most essential component of the “Central Dogma” which gives instructions to cells to synthesize proteins [1,2]. DNA is composed of a phosphate backbone, a sugar group, and four types of bases, those being guanine (G) and adenine (A) which are classified as purines, and thymine (T) and cytosine (C) which are classified as pyrimidines [3,4]. These four DNA bases are also involved in extracellular signaling pathways [5], as well as numerous metabolic pathways which result in the synthesis of various metabolites including energy carriers, the most notable being adenosine triphosphate (ATP) [6–8].

Several diseases may arise from the abnormal levels of DNA bases in blood including Lesch–Nyhan disease, gout, orotic aciduria, HIV/AIDS, epilepsy, and diseases which arise from genetic predispositions as well as some cancers [9–14]. Therefore, there is a need to sensitively measure the concentration of DNA bases in blood in order to clinically diagnose such diseases.

Traditionally, there are numerous analytical methods which can measure the concentration of DNA bases such as high-performance liquid chromatography with tandem mass spectroscopy (LC-MS/MS) [15–17], ultra-high performance liquid chromatography with tandem mass spectroscopy (ULC-MS/MS) [18,19], gas chromatography [20,21], capillary electrophoresis [22,23], Raman spectroscopy [24], as well as ultraviolet-visible (UV-vis) spectroscopy [25]. However, these techniques present various drawbacks such as the high cost of bench-top instruments, complex protocols requiring highly trained users, long times for sample pre-treatment and analysis [12–14].

Electrochemical sensors can function as platforms which overcome these drawbacks as they can be adapted to be highly portable, user-friendly, and cost-effective, and can be used as point of care devices for the rapid analysis of DNA bases. Oliveira-Brett et al. [26] elucidated the electrochemical oxidation mechanism for G and A using a glassy carbon electrode (GCE), they also developed an electrochemical sensor able to detect all four DNA bases over a wide range of pH [27]. Since then, several researchers developed electrochemical sensors for the detection of DNA bases using a wide variety of nanocomposites [28–31].

Furthermore, in recent years, there has been a push towards developing green, sustainable electrochemical sensors using a variety of materials [32–34]. Baby et al. [35] recently analyzed the use of various eutectic solvents to synthesize MgFe_2O_4 which was used as an electrocatalyst for the simultaneous determination of nitrofurantoin and 4-nitrophenol. Zaidi [36] successfully utilized 3-pyridine carboxylic acid amide (Nicotinamide), an environmentally friendly compound, as a functional monomer over reduced graphene oxide (rGO), which was used to detect adrenaline. Chaithra et al. [37] were able to synthesize biomass-derived carbon nanospheres from the leaves of *Mimosa pudica*, which were then incorporated with Pd nanoparticles for the electrochemical sensing of morin. Furthermore, there were recent reports of using biochar derived from sugarcane stalks which were successfully incorporated into biosensors [38,39]. Recent studies have also shown that sugarcane bagasse can be used as a sustainable bio-sorbent to remove methylene blue (MB) from wastewater polluted with the compound [40–42]. MB was frequently demonstrated to be a useful redox mediator that can amplify the detection of DNA hybridization [43,44]. Previous reports have also shown that MB displays specific affinity towards G bases [45]. Given these recent findings, our group was inspired to pursue the combination of sugarcane absorbed with MB and use it as an electrode modifier to develop a sensitive electrochemical sensor.

Recently, our group reported a carbon-based electrode modified with a graphene oxide (GO) and multi-walled carbon nanotube (MWCNT) nanocomposite [14], as well as the development of graphene oxide nanoribbons in chitosan [46], both for the simultaneous determination of DNA bases. Herein, we developed a graphite paste electrode (GPE), which incorporated the biochar from the bagasse of sugar canes along with methylene blue (MB), which was able to detect all four DNA bases with improved sensitivity over a wide linear range of concentrations using differential pulse voltammetry (DPV). The performance of the GPE with sugarcane biochar (SC) and methylene blue (GPE-SC-MB) was tested over a range of pH values and was also compared against a blank GPE, as well as against a GPE which incorporated only SC (GPE-SC). A scan rate study was performed to evaluate the electroactive surface area, as well as chronoamperometry to elucidate the diffusion coefficients for each DNA base. Finally, the modified electrode was compared with the existing sensors for DNA detection in the recent literature. The sensor was also tested in human saliva samples with satisfactory recovery values.

2. Materials and Methods

2.1. Reagents

The four DNA bases (G, A, T, and C), along with methylene blue (MB) ($\text{C}_{16}\text{H}_{18}\text{ClN}_3\text{S}\cdot x\text{H}_2\text{O}$), paraffin oil, potassium hexacyanoferrate (II) trihydrate ($\text{K}_4[\text{Fe}(\text{CN})_6]\cdot 3\text{H}_2\text{O}$), potassium hexacyanoferrate (III) ($\text{K}_3[\text{Fe}(\text{CN})_6]$), potassium chloride (KCl), hydrochloric acid (HCl), and sodium hydroxide (NaOH) were all purchased from Sigma-Aldrich (Oakville, ON, Canada). The electrolyte solutions of 0.2 M phosphate buffer ranging from a pH of 3.0 to 8.0 were made using 85% (*v/v*) phosphoric acid obtained from Fischer Scientific (Mississauga, ON, Canada), and the pH was adjusted using 10 M NaOH. Sugarcane stalks were purchased from a local vendor in Mississauga, ON, Canada. The four DNA base solutions (G and A were 0.01 M, T and C were 0.05 M) were made by dissolving each compound in deionized water in the presence of 100 μL of concentrated NaOH. All dilutions were performed using deionized water.

2.2. Instrumentation

Scanning electron microscopy (SEM) was performed using a Hitachi S530 Scanning electron microscope (Hitachi Ltd., Tokyo, Japan). All Fourier transform-infrared spectrums (FT-IR) were obtained using an Alpha Fourier transform infrared spectrometer (Bruker Corp., Billerica, MA, USA). The pH of electrolyte solutions was measured using a VWR SB70P pH meter. Electrochemical measurements were performed at room temperature using Autolab Potentiostat/Galvanostat (PGSTAT 302N, Metrohm AG, Herisau, Switzerland) in connection with NOVA™ software (NOVA 2.1.2, Metrohm AG, Herisau, Switzerland). The electrochemical cell was a three-electrode one where the working electrode was the GPE-SC-MB (unless stated otherwise), the counter electrode was platinum, and the reference electrode was a saturated silver/silver chloride (Ag/AgCl) electrode. All DPV measurements were recorded from +0.4 to +1.6 V at a step potential of 5 mV, a modulation amplitude of 25 mV, a modulation time of 0.05 s, and an interval time of 0.5 s. The redox probe solution of 10 mM $[\text{Fe}(\text{CN})_6]^{3-/4-}$ in 0.1 M KCl was used in electrochemical impedance spectroscopy (EIS) measurements. The Nyquist plots were obtained in a frequency range from 0.1 Hz to 10 kHz. NOVA™ software was used for the fitting and simulation of the obtained EIS plots using the modified Randles equivalent circuit.

2.3. Preparation of Methylene Blue-Modified Sugarcane Biochar (SC-MB)

Before activation, SC was washed with deionized water to remove any impurities and then cut to 5 cm pieces and dried at room temperature (RT) for 72 h. They were further dried to a constant weight in an oven at 110 °C for 12 h. Activation was carried out using a furnace at 500 °C with heating rate of 15 °C/min, for 2 h and then cooled to RT and milled for 2 h using a ball milling machine. The obtained product was named as sugarcane biochar (SC). A portion (5 g) of SC was mixed and shaken with 10 mL of a saturated MB solution for 24 h. The final product (SC-MB) filtered and washed with deionized water until the rinse was colorless. Finally, SC-MB samples were dried in an oven at 90 °C for 12 h.

2.4. Preparation of Graphite Paste Electrode (GPE) with SC-MB

The modified GPE with SC-MB was prepared using stoichiometric dilution by progressively mixing 4 mg of SC-MB with 196 mg of graphite powder. The mixture was homogenated and grounded in a ceramic mortar with a pestle for 10 min and then mixed with 5 mg of paraffin oil for another 10 min. The prepared paste was filled in 3 mm internal diameter glass tubes and a copper wire was used as the electrical connection. This modified electrode is denoted as GPE-SC-MB. The modified electrode with only SC was prepared in a similar manner using 4 mg of SC (2%, *w/w*) and denoted as GPE-SC in the absence of MB. Moreover, the method was also used for developing the bare GPE using only a mixture of graphite and paraffin oil in the absence of SC-MB. The latter two electrodes were used for comparison studies.

2.5. Human Saliva Samples

All experimental studies using human saliva were conducted following the ethical guidelines of the University of Toronto. The saliva sample was collected from a male volunteer and was stored in an ice bath prior to use. Six hundred (600) μL of the saliva sample was mixed with 2.4 mL of 0.2 M phosphate buffer (pH 7.0). The DNA base solutions were then sequentially added to the mixture to perform the electrochemical measurements.

3. Discussion

3.1. Characterization of GPE-SC-MB Nanocomposite

SEM was used to investigate the microscopic structure of the intact SC-MB hybrid nanocomposite (post-heating, before grinding) as shown in Figure 1A–D with different magnifications. As shown in Figure 1, the cell wall of the bagasse fibers provided ample surface area for the MB molecules to be adsorbed into the SC, providing an abundance of active sites for the electrochemical reactions to proceed with high electron transfer efficiency.

The arrows in Figure 1 indicate the micropores within the sugarcane structure that have been shown to be filled with MB during the adsorption process [41]. Previous literature shows that chemisorption is the dominant mechanism by which MB is attached to the surface of the sugarcane [41]. The structural morphology of the SC is also similar to that obtained from previous studies of sugar cane [47]. Although these SEM images were taken prior to the grinding of the SC-MB hybrid nanocomposite, our hypothesis is that the overall surface density of the MB on the SC surface was largely preserved, even though the grinding process might lead to the breakdown of the overall macrostructure of the SC. SEM images of the SC-MB hybrid nanocomposite after grinding are shown in Figure S1.

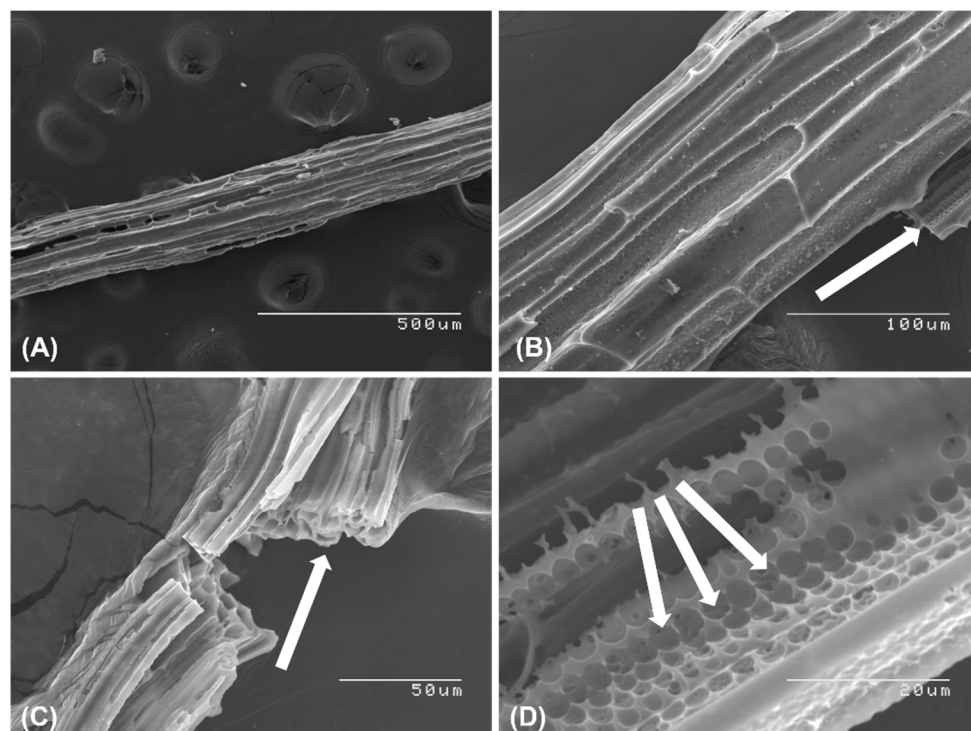


Figure 1. (A–D) SEM images of intact bagasse fibers treated with a saturated MB solution overnight which was used to develop the SC-MB hybrid nanocomposite. The scale bars in images (A–D) are 500 μm , 100 μm , 50 μm , and 20 μm , respectively. The arrows indicate the micropore structure within the SC.

Figure 2 shows the FT-IR of the SC-MB hybrid nanocomposite as well as the MB and SC separately. As shown, the spectrum of MB displayed peaks characteristic of the structure including a C=C stretch at $\sim 1490\text{ cm}^{-1}$, a C-H bend arising from the aromatic portion at $\sim 1590\text{ cm}^{-1}$, a sp^3 C-H stretch at $\sim 2920\text{ cm}^{-1}$, a sp^2 C-H stretch at $\sim 3020\text{ cm}^{-1}$, as well as the characteristic S-H stretch at $\sim 2690\text{ cm}^{-1}$ and a N-H stretch at $\sim 330\text{ cm}^{-1}$. All of these peaks for MB were in agreement with previous studies of the compound [48]. The FT-IR of the sugar cane also showed characteristic peaks of SC. This was demonstrated by the glycosidic β -(1 \rightarrow 4) at $\sim 890\text{ cm}^{-1}$, an asymmetrical C-O-C stretch at $\sim 110\text{ cm}^{-1}$, as well as a C=C stretch at $\sim 1560\text{ cm}^{-1}$ and a C-H bend at $\sim 1590\text{ cm}^{-1}$, both of which were indicative of an aromatic ring structure. The FT-IR spectrum of SC closely resembled those previously reported [47]. Furthermore, at the SC-MB spectra, several peaks characteristic of MB were observed such as the C-N stretching observed at $\sim 1578\text{ cm}^{-1}$, and the C-N stretching vibration due to the $-\text{N}(\text{CH}_3)_2^+$ at 1373 cm^{-1} , similar to the reports of previous studies [41], although these signals were somewhat weak, which was likely a result of the relatively low amount of MB that was adsorbed on SC. Recent research on the effects of MB adsorption onto SC corroborated this observation [40]. Although, further research is needed to determine why some MB peaks were absent or attenuated in the SC-MB spectrum, we

hypothesize that this might be due to the adsorption of MB deep within the micropores of the SC, a phenomenon referred to as “micropore filling” [41].

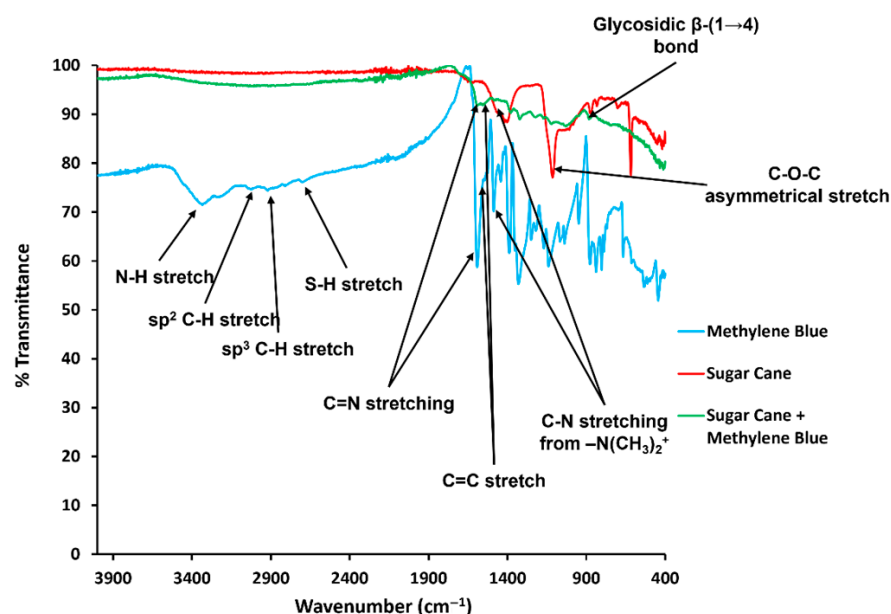


Figure 2. FT-IR spectra of MB (powder), SC, and the SC-MB hybrid nanocomposite.

3.2. Comparison of the Modified Electrodes

A comparison of different electrodes to evaluate their electroactivity with regards to the oxidation of the four DNA bases is shown in Figure 3A–D. The study compares a bare GPE, a GPE with 2% (*w/w*) SC (GPE-SC) and the GPE-SC-MB. Figure 3A–C shows the voltammograms of the GPE, GPE-SC, and GPE-SC-MB in the presence (solid line) and absence (dashed line) of the DNA bases. The three electrodes detected G, A, T, and C at the potentials of 0.67, 0.93, 1.12 and 1.28 V, respectively. Figure 3D shows an overlay of the GPE, GPE-SC, and GPE-SC-MB voltammograms in the presence of the DNA bases. Interestingly, the GPE-SC displayed a moderately improved sensitivity for the pyrimidines G and A, but a lower sensitivity for the purines, T and C, compared to the GPE. The GPE-SC-MB hybrid nanocomposite displayed improved sensitivity for all four DNA bases compared to the bare GPE and GPE-SC. Table 1 shows a comparison of the peak currents of obtained from all three electrodes.

Electrochemical impedance spectroscopy (EIS) was used as another comparison study and the results are shown in Figure 3E. The Nyquist plots for all electrodes contained two parts; (1) a semicircle at higher frequencies, where the diameter displayed the charge transfer resistance (R_{ct}), (2) a straight line, at lower frequencies which resulted due to the mass transfer limitations (W , Warburg element). The R_{ct} values of bare GPE, GPE-SC, GPE-SC-MB were 1024.9, 172.2, and 30.1 Ω , respectively. The R_{ct} for the GPE-SC and GPE-SC-MB were about 5.95 and 34.0-fold lower in comparison to the bare GPE, respectively. The low R_{ct} resulting from the addition of the SC and SC-MB to GPE showed an increase in the conductivity of the modified electrodes, due to the conductive nature of SC and SC-MB. This result emphasized the fact that both SC and SC-MB facilitated the electron transfer mechanism. Indeed, after using SC-MB as an electrode modifier in GPE, the R_{ct} was the lowest in comparison to bare GPE and GPE-SC. It can be ascribed to the adsorption of the MB on SC that acted as a mediator for rapid electron transfer.

Table 1. A comparison of the anodic peak current values observed using the bare GPE, GPE-SC, and GPE-SC-MB for four DNA bases G (33.3 μM), A (33.3 μM), T (333.3 μM) and C (333.3 μM) in 0.2 M phosphate buffer (pH 7.0).

	$I_{p,a}$ Guanine (μA)	$I_{p,a}$ Adenine (μA)	$I_{p,a}$ Thymine (μA)	$I_{p,a}$ Cytosine (μA)
GPE	6.83	6.04	3.80	4.28
GPE-SC	21.04	10.45	2.94	2.74
GPE-SC-MB	28.55	12.83	6.08	5.07

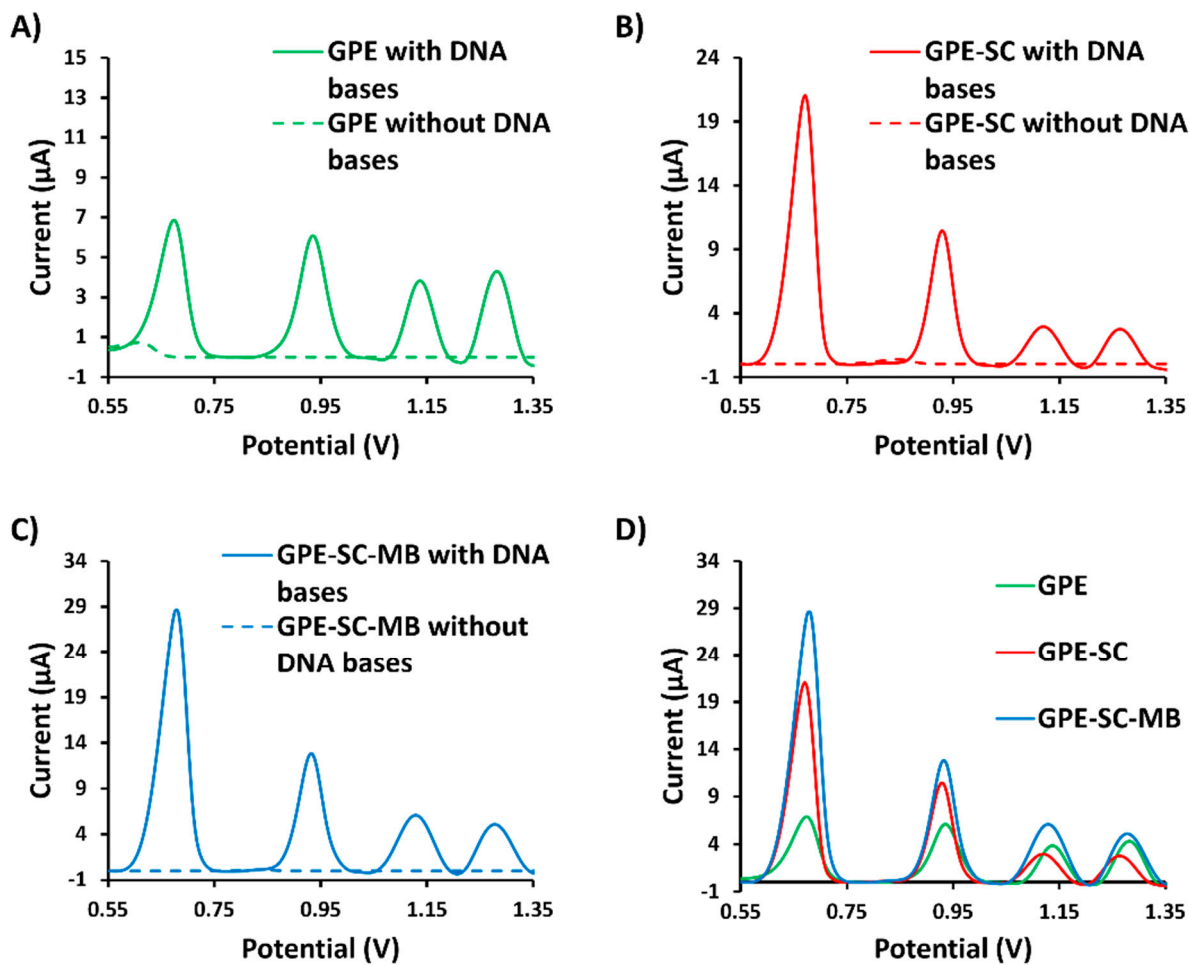


Figure 3. Cont.

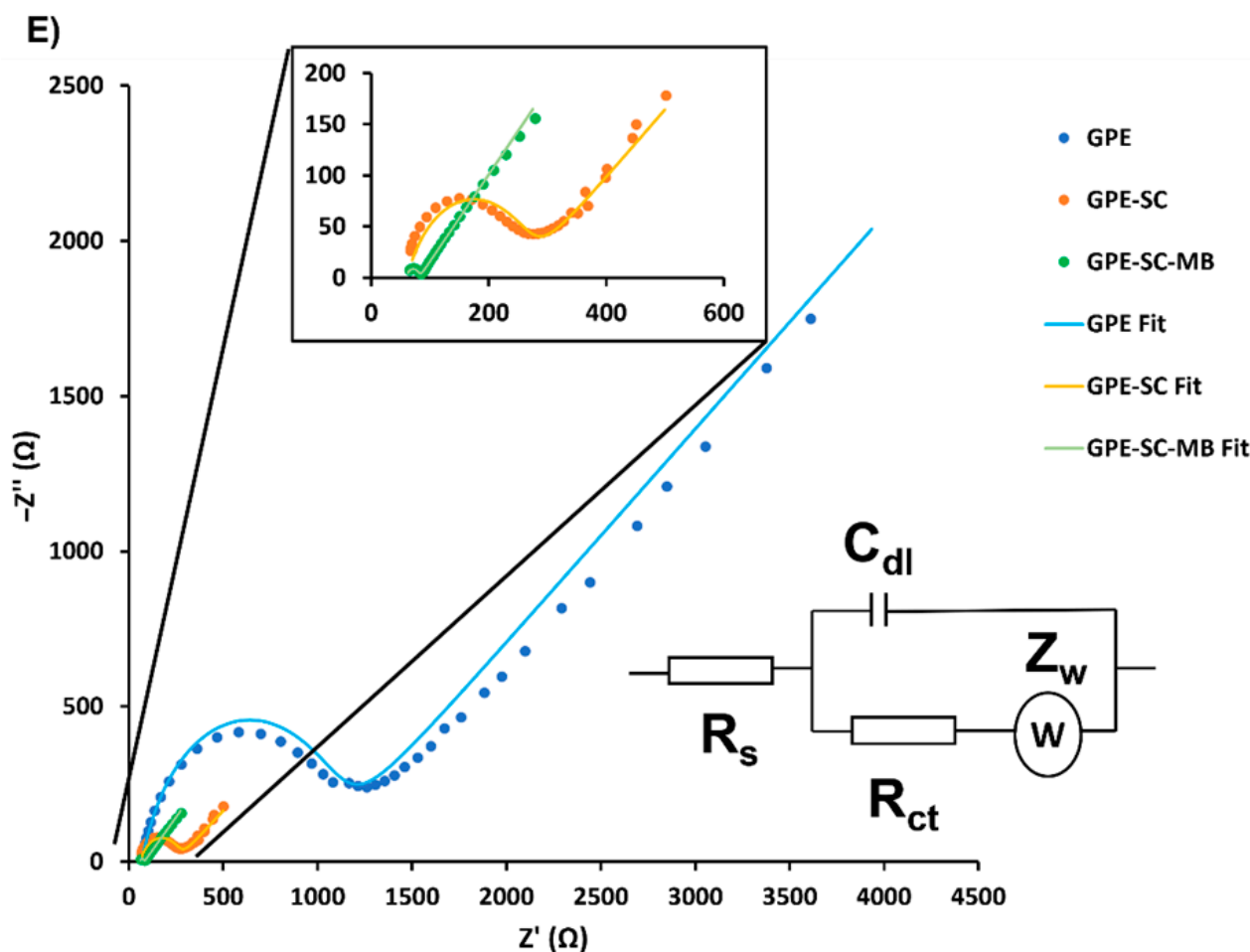


Figure 3. (A–C) Voltammograms of the GPE, GPE-SC, and GPE-SC-MB using DPV in the presence (solid line) and absence (dashed line) of the four DNA bases G (33.3 μ M), A (33.3 μ M), T (333.3 μ M) and C (333.3 μ M) in 0.2 M phosphate buffer (pH 7.0). (D) An overlay of the voltammograms of (A–C) comparing the performances of the GPE, GPE-SC, and GPE-SC-MB. (E) The Nyquist plots of GPE, GPE/SCC, GPE/SCC-MB. The inset shows the modified Randles equivalent circuit which was used to fit the Nyquist plots, where R_s , R_{ct} , C_{dl} and W represent the solution resistance, the charge transfer resistance, the double-layer capacitance and the Warburg element.

3.3. pH Effect and Reproducibility

The effect of varying the pH of the electrolyte on analyte detection was studied using DPV. This study served two purposes: first, it allowed for the determination of the optimum pH at which the sensor operated, and second, the oxidation mechanism of analytes could be determined by plotting the oxidation potential with respect to pH [14]. Figure 4A shows the results of the simultaneous determination of the DNA bases when the solution pH was varied from 3.0 to 8.0. Noticeably, the anodic peak potentials for each base shifted to a higher potential with respect to decreasing pH. As shown, all four bases display anodic peaks between pH 3.0 and 8.0 with varying sensitivity. Based on the magnitude of the current response for all four bases, the optimum pH to conduct the electrochemical detection of the analytes was determined as pH 7.0.

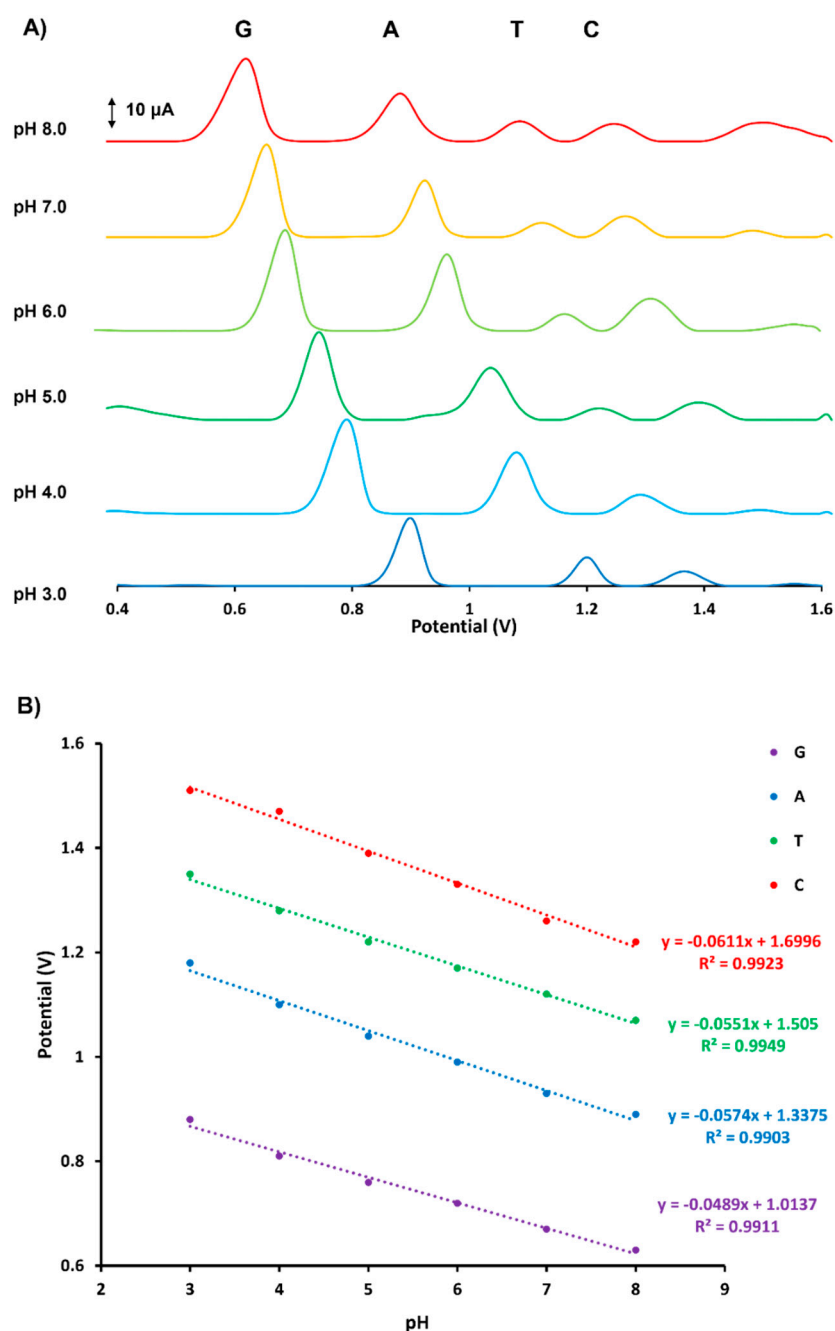
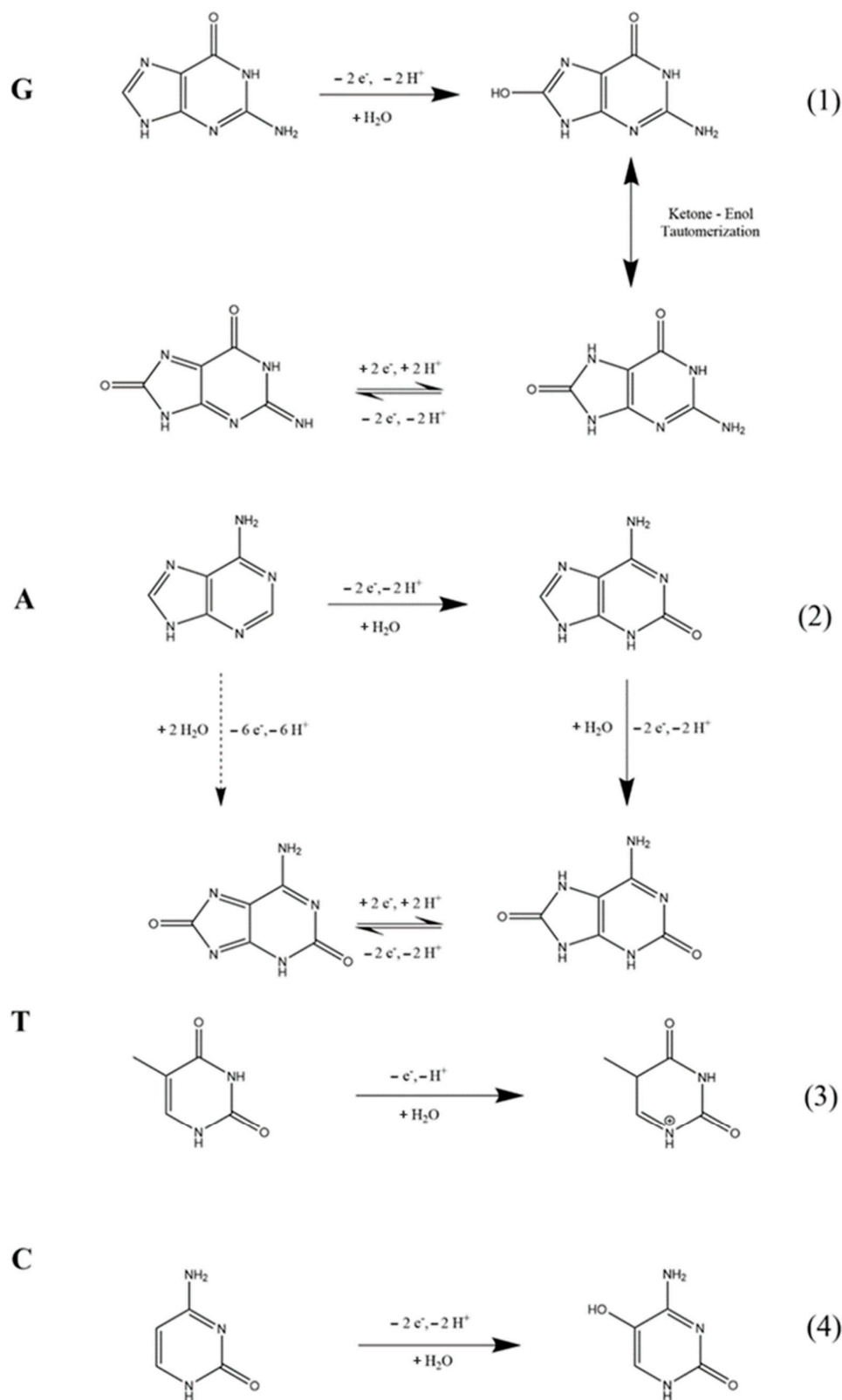


Figure 4. (A) Voltammograms obtained from the simultaneous electrochemical detection of the four DNA bases using DPV at varying pH conditions (pH 3.0, 4.0, 5.0, 6.0, 7.0 and 8.0). The concentrations of DNA bases were 33.3 μ M for G and A, and 333.3 μ M for T and C, and (B) plot showing the linear relationship between anodic peak potential and pH.

Figure 4B shows a plot of the relationship between oxidation potential and pH, with the equations representing those relationships. The slopes of the linear relationship between oxidation potential and pH were found to be 48.9, 57.4, 55.1, and 61.1 mV/pH for G, A, T, and C, respectively. Given these slopes were close to the Nernstian theoretical value of 59.1 mV/pH, it was deduced that the mechanisms for the electrochemical oxidation of the bases involved an exchange of an equal number of protons and electrons, which was in agreement with the previously cited literature [14,27]. Scheme 1 shows the oxidation mechanisms of DNA bases. For the oxidation of G, A, and C, the mechanism involved the exchange of two protons and electrons in the rate determining step (Scheme 1, (1), (2), and

(4)), while for T, the mechanism involved the exchange of only one proton and electron in the rate determining step (Scheme 1, (3)).



Scheme 1. The proposed oxidation mechanisms of the four DNA bases as deduced from studying the effect of pH on the anodic peak potential values.

Next, a reproducibility study was performed using the GC-SC-MB, where the concentration of all four DNA bases were kept constant for seven successive measurements ($n = 7$) (Figure S2). The RSD calculated for G, A, T, and C were 1.3%, 2.2%, 3.5% and 0.7%, respectively, indicating excellent reproducibility between measurements.

3.4. Calibration Plots for the Simultaneous Electrochemical Detection of DNA Bases

In order to assess the linear range of detection for the GPE-SC-MB, a calibration curve was developed by simultaneously spiking the four DNA bases into phosphate buffer (pH 7.0). Figure 5A shows the calibration curves developed for the four bases while Figure 5B–E shows the calibration plots for G, A, T, and C. Table 2 shows the equations that represent the linear ranges for all four analytes along with the regression coefficients for each equation, the limit of detection (LOD), and limit of quantification (LOQ) for each DNA base. Two separate linear ranges were detected for the detection of DNA bases as reported in prior electrochemical studies [49–53]. The linear ranges determined for G were from 0.67 to 20.0 μM for the first linear range and from 20.0 to 38.67 μM for the second linear range. The linear ranges for A were from 0.67 to 16 μM for the first linear range and from 16.0 to 126.67 μM for the second linear range. Prior studies have attributed the phenomenon of observing two linear ranges to be due to the low concentration of analyte molecules diffusing to the electroactive surfaces rapidly and resulting in a high response current. In contrast, at higher concentrations, some of the analyte molecules are adsorbed onto the electroactive surface that hinder the diffusion of incoming molecules, resulting in a different slope of calibration curve being generated at these high concentration ranges [53]. Only one linear range was observed for the purines T and C, which was also consistent with prior studies [14]. For both T and C, the linear range was from 6.67 to 1600 μM . To the best of our knowledge, this is the widest linear range reported for the detection of T and C (Table 3). Furthermore, the discrepancy between the pyrimidines (G and A), which displayed a relatively large current response with respect to concentration, and the purines (T and C), which displayed a relatively small current response with respect to concentration was attributed to the purines being more difficult to oxidize due to their inherent difficulty in donating electrons attributed to slower electron transfer rates [28]. Furthermore, it would be interesting for future experiments to determine the efficacy of the sensor in detecting DNA homopolymers such as polyadenine, polyguanine, polythymine, and polycytosine and whether their concentration can be determined based on the length of the polymer.

Table 2. Equations representing the linear plots for the four DNA bases along with their regression coefficients, LODs, and LOQs. ΔI_p refers to the current after background subtraction.

Analytes	Equations	R ²	LOD (μM)	LOQ (μM)
G	$\Delta I_{p(G1)} = 0.9330 [G] + 0.0347$	0.9967	0.037	0.12
	$\Delta I_{p(G2)} = 0.2565[G] + 14.008$	0.9927		
A	$\Delta I_{p(A1)} = 0.3230 [A] + 0.2496$	0.9901	0.042	0.14
	$\Delta I_{p(A2)} = 0.0715 [A] + 7.0113$	0.9919		
T	$\Delta I_{p(T)} = 0.0133 [T] + 0.0327$	0.9952	4.25	14.17
C	$\Delta I_{p(C)} = 0.0219 [C] + 0.5660$	0.9925	5.33	17.79

The LOD for each base was calculated using the equation $3SD/m$ where SD is the standard deviation of the current peaks from the background signals and m is the slope from the calibration plots. The LOD was 0.037 μM for G, 0.042 μM for A, 4.25 μM for T, and 5.33 μM for C. As shown in Table 3, these relatively low LODs in combination with the wide linear range for T and C suggested that this cost-effective, sustainable platform exhibited excellent sensitivity for the aforementioned bases. The LOQ for each DNA base

was calculated in a similar manner using the equation $10SD/m$ and are also shown in Table 2.

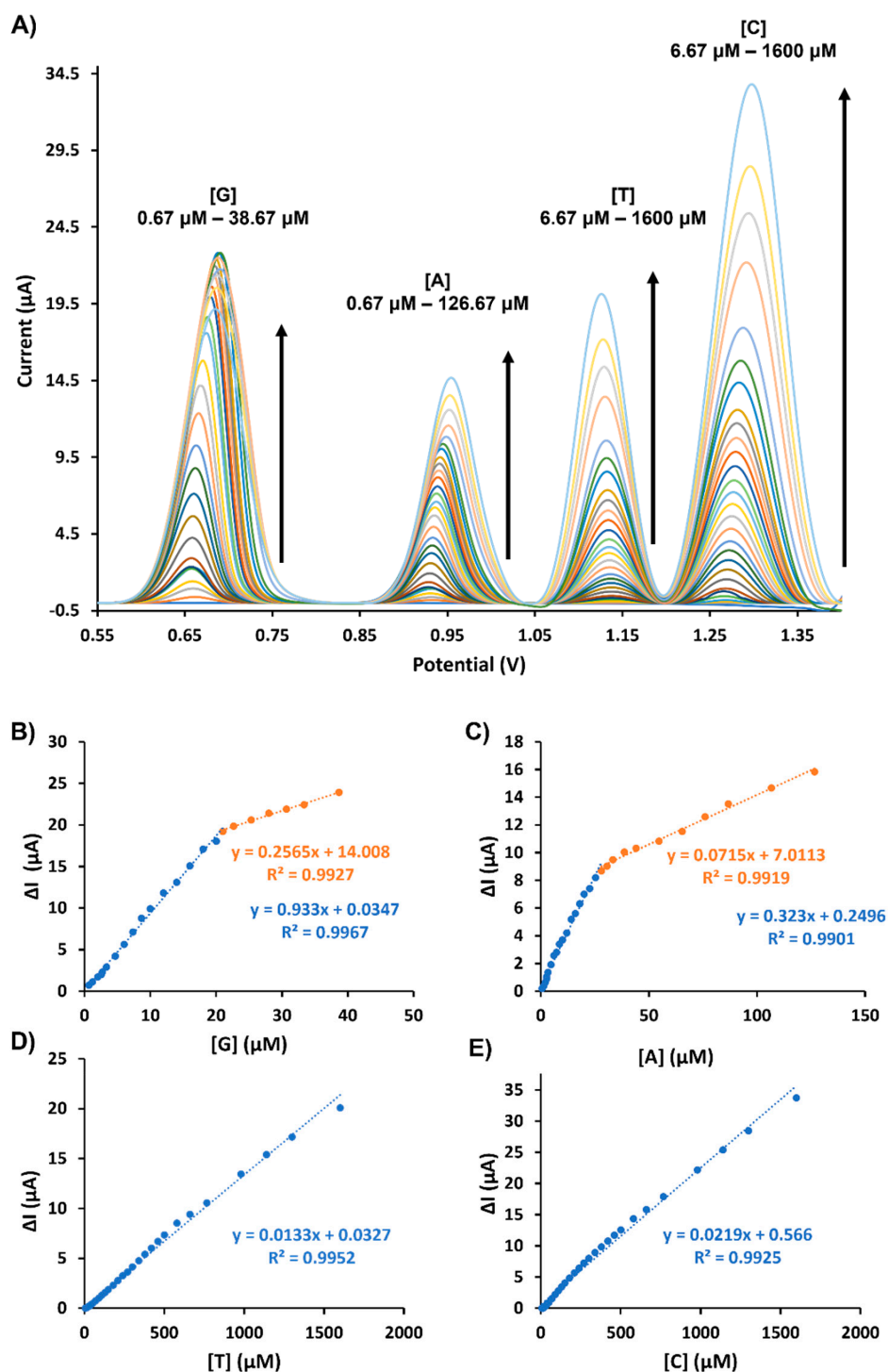


Figure 5. (A) An overlay of voltammograms representing the calibration curves for the simultaneous detection of G, A, T, and C using DPV at the GPE-SC-MB. Calibrations plots for (B) guanine, (C) adenine, (D) thymine, and (E) cytosine.

Table 3. Analytical performance comparison of this sensor with the ones reported in the recent literature.

Platform	Method	DNA Base	LOD (μM)	Linear Range (μM)	Reference
Graphene oxide nanoribbon in chitosan modified glassy carbon electrode (GCE)	GDPV	G	0.0018	0.013–256	[46]
		A	0.023	0.11–172	
		T	1.330	6.0–855	
		C	0.640	3.5–342	
Graphene oxide-MWCNT modified GCE	DPV	G	0.11	1–78	[14]
		A	0.43	2–119.5	
		T	1.71	12.5–227.5	
		C	0.80	5–132.5	
Graphitized mesoporous modified carbon paste electrode	DPV	G	0.76	25–200	[54]
		A	0.118	25–150	
Cu-Ni nanosphere decorated N,B-doped reduced graphene oxide-modified glassy carbon electrode (GCE)	DPV	G	0.118	1.0–160	[55]
		A	0.134	1.0–120	
MWCNT-Fe ₃ O ₄ polydopamine Ag-nanoparticle-modified carbon paste electrode	DPV	G	1.47	8–130	[56]
		A	5.66	10–120	
Graphene multilayer-modified GCE	DPV	G	0.3	2–120	[57]
		A	0.4	2–110	
		T	6.5	20–1100	
		C	4.5	20–1100	
MWCNT embedded with Au/reduced graphene oxide GPE	SWV	G	3.3	3–170	[28]
		A	3.7	3–190	
		T	7.9	7.5–800	
		C	9.0	9–900	
Graphene-Nafion™-modified GCE	DPV	G	0.58	2–120	[58]
		A	0.75	5–170	
2-(4-bromophenyl)-1-phenyl-1 <i>H</i> -phenanthro-[9,10- <i>d</i>]-imidazole-modified GCE	SWV	G	0.28	3–300	[13]
		A	0.24	1–300	
		T	3.2	30–800	
		C	6.8	20–750	
Boron-doped carbon nanospheres modified GCE	SWV	G	4×10^{-4}	0.01–0.5	[59]
		A	2×10^{-4}	0.01–0.5	
Copper metal-organic framework with reduced graphene oxide-modified GCE	DPV	G	0.012	0.02–100	[60]
		A	0.002	0.005–200	
MWCNT-COOH with a Cu -porphyrin metal covalent organic framework with Co nanoparticles on GCE	DPV	G	0.0055	0.04–130	[12]
		A	0.0072	0.06–130	
GPE-SC-MB	DPV	G	0.037	0.67–38.67	This work
		A	0.042	0.67–126.67	
		T	4.25	6.67–1600	
		C	5.33	6.67–1600	

3.5. Scan Rate

In order to calculate the active surface area of the electrodes, a scan rate study was performed by running CV experiments using successive scan rates in a solution containing an electroactive probe [14]. Figure S3A–C shows the cyclic voltammograms conducted using the GPE, GPE-SC, and GPE-SC-MB in a solution of 5 mM $K_3Fe(CN)_6$, 5 mM $K_4Fe(CN)_6$ with 0.1 M KCl. Figure S3D shows a plot of the current vs. the square root of the scan rate with respect to the anodic and cathodic current peaks for the bare GCE, GCE-SC and GCE-SC-MB. To calculate the electroactive surface area, the following Randles-Sevcik equation was used:

$$i_p = 2.69 \times 10^5 n^{\frac{3}{2}} A C_0 D^{\frac{1}{2}} v^{\frac{1}{2}}$$

where i_p is the current resulting from the $Fe(CN)_6^{3-/4-}$, n is the number of electrons exchanged (for $Fe(CN)_6^{3-/4-}$, $n = 1$), C_0 is 10^{-5} mol/cm³ (the concentration of $Fe(CN)_6^{3-/4-}$), v is the scan rate and D is the diffusion coefficient of $Fe(CN)_6^{3-/4-}$ which is 7.6×10^{-6} cm²·s⁻¹ [61]. The electroactive surface area (A) values were calculated as 0.557 cm², 0.753 cm², 1.629 cm² for GPE, GPE-SC, and GPE-SC-MB, respectively, indicating that the GPE-SC-MB had approximately 3-fold more the electroactive surface area than the bare GPE.

3.6. Chronoamperometry

The diffusion coefficient of the analytes was obtained using chronoamperometry at GPE-SC-MB and the results are shown in Figures S4–S7. All chronoamperograms were performed in a 0.2 M phosphate buffer (pH 7.0) with varying concentrations of the DNA bases. Based on these results, the diffusion coefficient (D) was determined for each analyte according to the Cottrell equation shown below:

$$i = \frac{nFAC\sqrt{D}}{\sqrt{(\pi t)}}$$

where i is the current in Amperes, n is the number of electrons exchanged, F is the Faraday's constant (96485 C/mol), A is the electroactive surface area calculated from the scan rate study, C is the concentration of the DNA base, and t is time in s. The diffusion coefficients of the DNA bases were determined as 4.04×10^{-5} , 1.27×10^{-5} , 3.12×10^{-6} , and 9.51×10^{-7} cm²/s for G, A, T, and C, respectively.

3.7. Real Samples

The performance of the GC-SC-MB for the simultaneous detection of the DNA bases was evaluated in a sample of human saliva using standard addition. The purpose of this study was to evaluate preliminarily whether the GC-SC-MB could maintain its performance in a real sample matrix. The saliva was diluted 5-fold with 0.2 M phosphate buffer (pH 7.0). The saliva was diluted as the effect of non-specific adsorption would be significant for a 100% saliva matrix. Unfortunately, the GC-SC-MB was unable to detect the DNA bases prior to spiking, likely due to the concentration of the native DNA bases being less than the LOD.

Once the saliva mixture was prepared, it was then spiked with known concentrations of G, A, T, and C (1.33–14.67 μM for G and A; 20–200 μM for T and C). The voltammograms obtained for the spiking of the real samples are shown in Figure S8. Given the lower concentrations used in this experiment when compared to the calibration curve generated in Figure 5A, the current generated from the electrooxidation of the DNA bases is expectedly lower. The detected concentrations were determined by using the calibration curves outlined above. The recovery values for each DNA base (12.0 μM for G and A; 146.7 μM for T and C) are shown in Table 4. The recovery values obtained were between 99 and 103% which indicated that the sensor had the potential of applications in clinical samples.

Table 4. Detected concentrations and the recovery for the simultaneous detection of the four DNA bases using the GC-SC-MB (n = 3).

Sample Matrix	DNA Base	Spiked Concentration (μM)	Detected Concentration \pm S.D. (μM)	% Recovery \pm %RSD
Human Saliva	G	12.0	12.3 \pm 0.2	102.5 \pm 1.7
	A	12.0	12.1 \pm 0.3	100.8 \pm 2.5
	T	146.7	145.7 \pm 0.7	99.3 \pm 0.5
	C	146.7	149.1 \pm 0.6	101.7 \pm 0.4

4. Conclusions

In this study, a sustainable GPE was constructed using biochar from sugarcane bagasse soaked in a solution of MB which was successfully employed to simultaneously detect G, A, T, and C. Compared to the previous electrochemical platforms, this electrode showed a relatively wide linear range of detection and low LOD. Furthermore, the electrochemical sensor was tested in various phosphate buffers of different pH to elucidate the electrochemical oxidation mechanism of the four DNA bases. By varying the scan rate, it was determined that the electroactive surface area of the modified electrode was 1.629 cm². Furthermore, chronoamperometry measurements were performed to determine the diffusion coefficient of each DNA base. Finally, the electrode was tested in a real sample matrix of human saliva samples which showed promising % recovery values indicating its potential to be used in a clinical setting as a diagnostic tool. Future studies should focus on further optimizing this sensor for analyzing more complex sample matrix such as blood and 100% saliva such that the sensor can be ultimately developed to be a point-of-care diagnostic test for patients with who suspect to be experiencing diseases with abnormal levels of DNA bases. Furthermore, given the sustainable material used to create the sensor, further research should be conducted to develop other point-of-care tests using similarly sourced material.

Supplementary Materials: The following supporting information can be downloaded at: <https://www.mdpi.com/article/10.3390/chemosensors11030169/s1>, Figure S1: SEM images of the SC-MB nanocomposite after grinding; Figure S2: reproducibility study with seven successive DPV measurements; Figure S3: scan rate dependence study; Figure S4: chronoamperograms of the GC-SC-MB in the presence of varying concentrations of guanine for the calculation of diffusion constant; Figure S5: chronoamperograms of the GC-SC-MB in the presence of varying concentrations of adenine for the calculation of diffusion constant; Figure S6: chronoamperograms of the GC-SC-MB in the presence of varying concentrations of thymine for the calculation of diffusion constant; Figure S7: chronoamperograms of the GC-SC-MB in the presence of varying concentrations of cytosine for the calculation of diffusion constant; Figure S8: differential pulse voltammograms showing the standard addition study in saliva samples.

Author Contributions: Conceptualization, Q.H., Z.M., M.N. and K.K.; methodology, Z.M. and M.N.; writing—original draft preparation, Q.H., M.N. and K.K.; writing—review and editing, Q.H., M.N. and K.K.; visualization, Q.H.; supervision, M.N. and K.K.; project administration, M.N. and K.K.; funding acquisition, K.K. All authors have read and agreed to the published version of the manuscript.

Funding: This work was supported by the Canada Research Chair Tier-2 award to K. Kerman for “Bioelectrochemistry of Proteins” (project no. 950-231116), the Ontario Ministry of Research and Innovation (Project no. 35272), Discovery Grant (project no. RGPIN-2020-07164) from the Natural Sciences and Engineering Research Council of Canada (NSERC), and the Canada Foundation for Innovation (project no. 35272).

Institutional Review Board Statement: Not applicable.

Informed Consent Statement: Not applicable.

Data Availability Statement: The data presented in this study are available on request from the corresponding author.

Acknowledgments: The authors would like to thank the Centre for the Neurobiology of Stress in the University of Toronto Scarborough for their technical assistance with SEM studies. The authors would also like to thank the TRACES centre at UTSC for their assistance with the FT-IR studies.

Conflicts of Interest: The authors declare no conflict of interest.

References

1. Cobb, M. 60 Years Ago, Francis Crick Changed the Logic of Biology. *PLoS Biol.* **2017**, *15*, e2003243. [[CrossRef](#)] [[PubMed](#)]
2. Crick, F. Central Dogma of Molecular Biology. *Nature* **1970**, *227*, 561–562. [[CrossRef](#)]
3. Soukup, G.A. Nucleic Acids: General Properties. In *Encyclopedia of Life Sciences*; Wiley & Sons: Hoboken, NJ, USA, 2003. [[CrossRef](#)]
4. Crick, F.; Watson, J. Molecular Structure of Nucleic Acids. *Nature* **1953**, *171*, 737–738.
5. Idzko, M.; Ferrari, D.; Riegel, A.K.; Eltzschig, H.K. Extracellular Nucleotide and Nucleoside Signaling in Vascular and Blood Disease. *Blood* **2014**, *124*, 1029–1037. [[CrossRef](#)] [[PubMed](#)]
6. Dudzinska, W.; Lubkowska, A.; Dolegowska, B.; Safranow, K.; Jakubowska, K. Adenine, Guanine and Pyridine Nucleotides in Blood during Physical Exercise and Restitution in Healthy Subjects. *Eur. J. Appl. Physiol.* **2010**, *110*, 1155–1162. [[CrossRef](#)] [[PubMed](#)]
7. Moffatt, B.A.; Ashihara, H. Purine and Pyrimidine Nucleotide Synthesis and Metabolism. *Arab. B.* **2002**, *1*, e0018. [[CrossRef](#)]
8. Peplinska-Miaskowska, J.; Wichowicz, H.; Smolenski, R.T.; Jablonska, P.; Kaska, L. Comparison of Plasma Nucleotide Metabolites and Amino Acids Pattern in Patients with Binge Eating Disorder and Obesity. *Nucl. Nucl. Nucleic Acids* **2020**, *40*, 32–42. [[CrossRef](#)]
9. Kelley, R.E.; Andersson, H.C. *Disorders of Purines and Pyrimidines*, 1st ed.; Elsevier: Amsterdam, The Netherlands, 2014; Volume 120.
10. Fumagalli, M.; Lecca, D.; Abbracchio, M.P.; Ceruti, S. Pathophysiological Role of Purines and Pyrimidines in Neurodevelopment: Unveiling New Pharmacological Approaches to Congenital Brain Diseases. *Front. Pharmacol.* **2017**, *8*, 941. [[CrossRef](#)]
11. Traut, T.W. Physiological Concentrations of Purines and Pyrimidines. *Mol. Cell. Biochem.* **1994**, *140*, 1–22. [[CrossRef](#)]
12. Wang, M.; Guo, H.; Xue, R.; Guan, Q.; Zhang, J.; Zhang, T.; Sun, L.; Yang, F.; Yang, W. A Novel Electrochemical Sensor Based on MWCNTs-COOH/Metal-Covalent Organic Frameworks (MCOFs)/Co NPs for Highly Sensitive Determination of DNA Base. *Microchem. J.* **2021**, *167*, 106336. [[CrossRef](#)]
13. Lu, N.; Liu, H.; Huang, R.; Gu, Y.; Yan, X.; Zhang, T.; Xu, Z.; Xu, H.; Xing, Y.; Song, Y.; et al. Charge Transfer Platform and Catalytic Amplification of Phenanthroimidazole Derivative: A New Strategy for DNA Bases Recognition. *Anal. Chem.* **2019**, *91*, 11938–11945. [[CrossRef](#)] [[PubMed](#)]
14. Wang, S.; Ferrag, C.; Noroozifar, M.; Kerman, K. Simultaneous Determination of Four DNA Bases at Graphene Oxide/Multi-Walled Carbon Nanotube Nanocomposite-Modified Electrode. *Micromachines* **2020**, *11*, 294. [[CrossRef](#)] [[PubMed](#)]
15. Huang, Q.; Kaiser, K.; Benner, R. A Simple High Performance Liquid Chromatography Method for the Measurement of Nucleobases and the RNA and DNA Content of Cellular Material. *Limnol. Oceanogr. Methods* **2012**, *10*, 608–616. [[CrossRef](#)]
16. Muguruma, Y.; Tsutsui, H.; Akatsu, H.; Inoue, K. Comprehensive Quantification of Purine and Pyrimidine Metabolism in Alzheimer's Disease Postmortem Cerebrospinal Fluid by LC-MS/MS with Metal-Free Column. *Biomed. Chromatogr.* **2020**, *34*. [[CrossRef](#)] [[PubMed](#)]
17. Stentoft, C.; Vestergaard, M.; Løvendahl, P.; Kristensen, N.B.; Moorby, J.M.; Jensen, S.K. Simultaneous Quantification of Purine and Pyrimidine Bases, Nucleosides and Their Degradation Products in Bovine Blood Plasma by High Performance Liquid Chromatography Tandem Mass Spectrometry. *J. Chromatogr. A* **2014**, *1356*, 197–210. [[CrossRef](#)]
18. Laourdakis, C.D.; Merino, E.F.; Neilson, A.P.; Cassera, M.B. Comprehensive Quantitative Analysis of Purines and Pyrimidines in the Human Malaria Parasite Using Ion-Pairing Ultra-Performance Liquid Chromatography-Mass Spectrometry. *J. Chromatogr. B Anal. Technol. Biomed. Life Sci.* **2014**, *967*, 127–133. [[CrossRef](#)]
19. Liu, C.; Gu, C.; Huang, W.; Sheng, X.; Du, J.; Li, Y. Targeted UPLC-MS/MS High-Throughput Metabolomics Approach to Assess the Purine and Pyrimidine Metabolism. *J. Chromatogr. B Anal. Technol. Biomed. Life Sci.* **2019**, *1113*, 98–106. [[CrossRef](#)]
20. Brohi, R.O.Z.; Khuhawar, M.Y.; Channa, A.; Laghari, A.J.; Abbasi, K. Gas Chromatographic Determination of Purines and Pyrimidines from DNA Using Ethyl Chloroformate as Derivatizing Reagent. *Pak. J. Anal. Environ. Chem.* **2016**, *17*, 50–57. [[CrossRef](#)]
21. Brohi, R.O.Z.Z.; Khuhawar, M.Y.; Khuhawar, T.M.J. GC-FID Determination of Nucleobases Guanine, Adenine, Cytosine, and Thymine from DNA by Pre-column Derivatization with Isobutyl Chloroformate. *J. Anal. Sci. Technol.* **2016**, *7*, 5. [[CrossRef](#)]
22. Wang, P.; Ren, J. Separation of Purine and Pyrimidine Bases by Capillary Electrophoresis Using β -Cyclodextrin as an Additive. *J. Pharm. Biomed. Anal.* **2004**, *34*, 277–283. [[CrossRef](#)]
23. Friedeck, D.; Adam, T.; Bartk, P. Capillary Electrophoresis for Detection of Inherited Disorders of Purine and Pyrimidine Metabolism: A Selective Approach. *Electrophoresis* **2002**, *23*, 565–571. [[CrossRef](#)]
24. Carrillo-Carrión, C.; Armenta, S.; Simonet, B.M.; Valcárcel, M.; Lendl, B. Determination of Pyrimidine and Purine Bases by Reversed-Phase Capillary Liquid Chromatography with at-Line Surface-Enhanced Raman Spectroscopic Detection Employing a Novel SERS Substrate Based on ZnS/CdSe Silver-Quantum Dots. *Anal. Chem.* **2011**, *83*, 9391–9398. [[CrossRef](#)] [[PubMed](#)]
25. Cavalieri, L.F.; Bendich, A.; Tinker, J.F.; Brown, G.B. Ultraviolet Absorption Spectra of Purines, Pyrimidines, and Triazolopyrimidines. *J. Am. Chem. Soc.* **1948**, *70*, 3875–3880. [[CrossRef](#)] [[PubMed](#)]

26. Oliveira-Brett, A.M.; Diculescu, V.; Piedade, J.A.P. Electrochemical Oxidation Mechanism of Guanine and Adenine Using a Glassy Carbon Microelectrode. *Bioelectrochemistry* **2002**, *55*, 61–62. [[CrossRef](#)]
27. Oliveira-Brett, A.M.; Piedade, J.A.P.; Silva, L.A.; Diculescu, V.C. Voltammetric Determination of All DNA Nucleotides. *Anal. Biochem.* **2004**, *332*, 321–329. [[CrossRef](#)]
28. Ng, K.L.; Khor, S.M. Graphite-Based Nanocomposite Electrochemical Sensor for Multiplex Detection of Adenine, Guanine, Thymine, and Cytosine: A Biomedical Prospect for Studying DNA Damage. *Anal. Chem.* **2017**, *89*, 10004–10012. [[CrossRef](#)]
29. Anu Prathap, M.U.; Srivastava, R.; Satpati, B. Simultaneous Detection of Guanine, Adenine, Thymine, and Cytosine at Polyani-line/MnO₂ Modified Electrode. *Electrochim. Acta* **2013**, *114*, 285–295. [[CrossRef](#)]
30. Geng, X.; Bao, J.; Huang, T.; Wang, X.; Hou, C.; Hou, J.; Samalo, M.; Yang, M.; Huo, D. Electrochemical Sensor for the Simultaneous Detection of Guanine and Adenine Based on a PPyox/MWNTs-MoS₂ Modified Electrode. *J. Electrochem. Soc.* **2019**, *166*, B498–B504. [[CrossRef](#)]
31. Wang, P.; Wu, H.; Dai, Z.; Zou, X. Simultaneous Detection of Guanine, Adenine, Thymine and Cytosine at Choline Monolayer Supported Multiwalled Carbon Nanotubes Film. *Biosens. Bioelectron.* **2011**, *26*, 3339–3345. [[CrossRef](#)]
32. Sfragano, P.S.; Laschi, S.; Palchetti, I. Sustainable Printed Electrochemical Platforms for Greener Analytics. *Front. Chem.* **2020**, *8*, 644. [[CrossRef](#)]
33. Geetha Bai, R.; Muthoosamy, K.; Zhou, M.; Ashokkumar, M.; Huang, N.M.; Manickam, S. Sonochemical and Sustainable Synthesis of Graphene-Gold (G-Au) Nanocomposites for Enzymeless and Selective Electrochemical Detection of Nitric Oxide. *Biosens. Bioelectron.* **2017**, *87*, 622–629. [[CrossRef](#)] [[PubMed](#)]
34. Kalambate, P.K.; Rao, Z.; Dhanjai, Z.; Wu, J.; Shen, Y.; Boddula, R.; Huang, Y. Electrochemical (Bio) Sensors Go Green. *Biosens. Bioelectron.* **2020**, *163*, 112270. [[CrossRef](#)] [[PubMed](#)]
35. Baby, J.N.; Sriram, B.; Wang, S.F.; George, M. Effect of Various Deep Eutectic Solvents on the Sustainable Synthesis of MgFe₂O₄ Nanoparticles for Simultaneous Electrochemical Determination of Nitrofurantoin and 4-Nitrophenol. *ACS Sustain. Chem. Eng.* **2020**, *8*, 1479–1486. [[CrossRef](#)]
36. Zaidi, S.A. Utilization of an Environmentally-Friendly Monomer for an Efficient and Sustainable Adrenaline Imprinted Electrochemical Sensor Using Graphene. *Electrochim. Acta* **2018**, *274*, 370–377. [[CrossRef](#)]
37. Chaithra, C.; Bhat, V.S.; Akshaya, A.K.; Maiyalagan, T.; Hegde, G.; Varghese, A.; George, L. Unique Host Matrix to Disperse Pd Nanoparticles for Electrochemical Sensing of Morin: Sustainable Engineering Approach. *ACS Biomater. Sci. Eng.* **2020**, *6*, 5264–5273. [[CrossRef](#)]
38. He, L.; Yang, Y.; Kim, J.; Yao, L.; Dong, X.; Li, T.; Piao, Y. Multi-Layered Enzyme Coating on Highly Conductive Magnetic Biochar Nanoparticles for Bisphenol A Sensing in Water. *Chem. Eng. J.* **2020**, *384*, 123276. [[CrossRef](#)]
39. Liu, Y.; Yao, L.; He, L.; Liu, N.; Piao, Y. Electrochemical Enzyme Biosensor Bearing Biochar Nanoparticle as Signal Enhancer for Bisphenol a Detection in Water. *Sens. (Switz.)* **2019**, *19*, 1619. [[CrossRef](#)]
40. Al-Mokhalelati, K.; Al-Bakri, I.; Al Shibeh Al Wattar, N. Adsorption of Methylene Blue onto Sugarcane Bagasse-Based Adsorbent Materials. *J. Phys. Org. Chem.* **2021**, *34*, e4193. [[CrossRef](#)]
41. Zhou, F.; Li, K.; Hang, F.; Zhang, Z.; Chen, P.; Wei, L.; Xie, C. Efficient Removal of Methylene Blue by Activated Hydrochar Prepared by Hydrothermal Carbonization and NaOH Activation of Sugarcane Bagasse and Phosphoric Acid. *RSC Adv.* **2022**, *12*, 1885–1896. [[CrossRef](#)]
42. Siqueira, T.C.A.; da Silva, I.Z.; Rubio, A.J.; Bergamasco, R.; Gasparotto, F.; Paccola, E.A.d.S.; Yamaguchi, N.U. Sugarcane Bagasse as an Efficient Biosorbent for Methylene Blue Removal: Kinetics, Isotherms and Thermodynamics. *Int. J. Environ. Res. Public Health* **2020**, *17*, 526. [[CrossRef](#)]
43. Erdem, A.; Kerman, K.; Meric, B.; Akarca, U.S.; Ozsoz, M. Novel Hybridization Indicator Methylene Blue for the Electrochemical Detection of Short DNA Sequences Related to the Hepatitis B Virus. *Anal. Chim. Acta* **2000**, *422*, 139–149. [[CrossRef](#)]
44. Kara, P.; Kerman, K.; Ozkan, D.; Meric, B.; Erdem, A.; Ozkan, Z.; Ozsoz, M. Electrochemical Genosensor for the Detection of Interaction between Methylene Blue and DNA. *Electrochem. Commun.* **2002**, *4*, 705–709. [[CrossRef](#)]
45. Yang, W.; Ozsoz, M.; Hibbert, D.B.; Gooding, J.J. Evidence for the Direct Interaction between Methylene Blue and Guanine Bases Using DNA-Modified Carbon Paste Electrodes. *Electroanalysis* **2002**, *14*, 1299–1302. [[CrossRef](#)]
46. Zhou, J.; Li, S.; Noroozifar, M.; Kerman, K. Graphene Oxide Nanoribbons in Chitosan for Simultaneous Electrochemical Detection of Guanine, Adenine, Thymine and Cytosine. *Biosensors* **2020**, *10*, 30. [[CrossRef](#)]
47. Chandel, A.K.; Antunes, F.A.F.; Anjos, V.; Bell, M.J.V.; Rodrigues, L.N.; Polikarpov, I.; De Azevedo, E.R.; Bernardinelli, O.D.; Rosa, C.A.; Pagnocca, F.C.; et al. Multi-Scale Structural and Chemical Analysis of Sugarcane Bagasse in the Process of Sequential Acid-Base Pretreatment and Ethanol Production by *Scheffersomyces Shehatae* and *Saccharomyces Cerevisiae*. *Biotechnol. Biofuels* **2014**, *7*, 63. [[CrossRef](#)]
48. Khan, S.; Alam, F.; Azam, A.; Khan, A.U. Gold Nanoparticles Enhance Methylene Blue-Induced Photodynamic Therapy: A Novel Therapeutic Approach to Inhibit *Candida Albicans* Biofilm. *Int. J. Nanomed.* **2012**, *7*, 3245–3257. [[CrossRef](#)]
49. Li, S.; Noroozifar, M.; Kerman, K. Nanocomposite of Ferricyanide-Doped Chitosan with Multi-Walled Carbon Nanotubes for Simultaneous Senary Detection of Redox-Active Biomolecules. *J. Electroanal. Chem.* **2019**, *849*, 113376. [[CrossRef](#)]
50. Ganesh, H.; Noroozifar, M.; Kerman, K. Epigallocatechin Gallate-Modified Graphite Paste Electrode for Simultaneous Detection of Redox-Active Biomolecules. *Sensors* **2017**, *18*, 23. [[CrossRef](#)]

51. Zhang, S.; Li, B.Q.; Zheng, J. Bin an Electrochemical Sensor for the Sensitive Determination of Nitrites Based on Pt-PANI-Graphene Nanocomposites. *Anal. Methods* **2015**, *7*, 8366–8372. [[CrossRef](#)]
52. Dai, Z.; Chen, J.; Yan, F.; Ju, H. Electrochemical Sensor for Immunoassay of Carcinoembryonic Antigen Based on Thionine Monolayer Modified Gold Electrode. *Cancer Detect. Prev.* **2005**, *29*, 233–240. [[CrossRef](#)]
53. Li, B.Q.; Nie, F.; Sheng, Q.L.; Zheng, J. Bin An Electrochemical Sensor for Sensitive Determination of Nitrites Based on Ag-Fe₃O₄-Graphene Oxide Magnetic Nanocomposites. *Chem. Pap.* **2015**, *69*, 911–920. [[CrossRef](#)]
54. Thangaraj, R.; Senthil Kumar, A. Simultaneous Detection of Guanine and Adenine in DNA and Meat Samples Using Graphitized Mesoporous Carbon Modified Electrode. *J. Solid State Electrochem.* **2013**, *17*, 583–590. [[CrossRef](#)]
55. Lei, P.; Zhou, Y.; Zhu, R.; Liu, Y.; Dong, C.; Shuang, S. Novel Strategy of Electrochemical Analysis of DNA Bases with Enhanced Performance Based on Copper–nickel Nanosphere Decorated N,B–doped Reduced Graphene Oxide. *Biosens. Bioelectron.* **2020**, *147*, 111735. [[CrossRef](#)] [[PubMed](#)]
56. Yari, A.; Derki, S. New MWCNT-Fe₃O₄@PDA-Ag Nanocomposite as a Novel Sensing Element of an Electrochemical Sensor for Determination of Guanine and Adenine Contents of DNA. *Sens. Actuators B Chem.* **2016**, *227*, 456–466. [[CrossRef](#)]
57. Qin, J.; Gao, S.; Li, H.; Li, C.; Li, M. Growth of Monolayer and Multilayer Graphene on Glassy Carbon Electrode for Simultaneous Determination of Guanine, Adenine, Thymine, and Cytosine. *J. Electroanal. Chem.* **2021**, *895*, 115403. [[CrossRef](#)]
58. Yin, H.; Zhou, Y.; Ma, Q.; Ai, S.; Ju, P.; Zhu, L.; Lu, L. Electrochemical Oxidation Behavior of Guanine and Adenine on Graphene-Nafion Composite Film Modified Glassy Carbon Electrode and the Simultaneous Determination. *Process Biochem.* **2010**, *45*, 1707–1712. [[CrossRef](#)]
59. Emran, M.Y.; El-Safty, S.A.; Selim, M.M.; Shenashen, M.A. Selective Monitoring of Ultra-Trace Guanine and Adenine from Hydrolyzed DNA Using Boron-Doped Carbon Electrode Surfaces. *Sens. Actuators B Chem.* **2021**, *329*, 129192. [[CrossRef](#)]
60. Wang, X.; Zhang, J.; Wei, Y.; Xing, T.; Cao, T.; Wu, S.; Zhu, F. A Copper-Based Metal-Organic Framework/Graphene Nanocomposite for the Sensitive and Stable Electrochemical Detection of DNA Bases. *Analyst* **2020**, *145*, 1933–1942. [[CrossRef](#)]
61. Rajabi, H.; Noroozifar, M.; Khorasani-Motlagh, M. Graphite Paste Electrode Modified with Lewatit®FO36 Nano-Resin for Simultaneous Determination of Ascorbic Acid, Acetaminophen and Tryptophan. *Anal. Methods* **2016**, *8*, 1924–1934. [[CrossRef](#)]

Disclaimer/Publisher’s Note: The statements, opinions and data contained in all publications are solely those of the individual author(s) and contributor(s) and not of MDPI and/or the editor(s). MDPI and/or the editor(s) disclaim responsibility for any injury to people or property resulting from any ideas, methods, instructions or products referred to in the content.